High-performance type II WSO_x/WS_2-based heterojunction photodetectors

shi, Weiqi; Ding, Yifang; Fang, Shaojun; Zhou, Hong; Qi, Jiao; Fan, Jiajie; Zhang, Rongjun; Zhang, Guoqi; Tang, Hongyu

DOI
10.1016/j.apsusc.2024.161848

Publication date
2025

Document Version
Final published version

Published in
Applied Surface Science

Applied Surface Science 683 (2025) 161848

Contents lists available at ScienceDirect

Applied Surface Science

journal homepage: www.elsevier.com/locate/apsusc

Full Length Article

High-performance type II WSO_x/WS_2-based heterojunction photodetectors

Weiqi shi [a], Yifang Ding [b], Shaojun Fang [a], Hong Zhou [a], Jiao Qi [b], Jiajie Fan [a], Rongjun Zhang [a,b,*], Guoqi Zhang [c], Hongyu Tang [a,*]

[a] Academy for Engineering and Technology, Fudan University, Shanghai 200433, China
[b] Department of Optical Science and Engineering, Key Laboratory of Micro and Nano Photonic Structures (MOE), Shanghai Engineering Research Center of Ultra-Precision Optical Manufacturing, Fudan University, Shanghai 200433, China
[c] EEMCS Faculty, Delft University of Technology, Delft 2628CD, the Netherlands

ARTICLE INFO

Keywords:
2D materials
Van der Waals heterostructures
WSO_x/WS_2
Photodetectors
First-principles analysis

ABSTRACT

Van der Waals heterojunctions (vdWHs) have garnered significant attention for their promising applications in optoelectronics, attributed to their exceptional physical attributes. In this study, we present a straightforward approach to fabricating high-performance vdWHs photodetectors. Specifically, we prepared WSO_x/WS_2 vdWH photodetectors through the ozone oxidation of a WS_2 thin films at 100 °C. To characterize the morphology and optical properties of both the WS_2 and WSO_x/WS_2 thin films, we utilized atomic force microscopy (AFM) and Raman spectroscopy. Additionally, X-ray photoelectron spectroscopy (XPS) was employed to delve into the structural evolution by scrutinizing the bonding states of W, O, and S in the WS_2 before and after the ozone oxidation process. The resultant WSO_x/WS_2 vdWH photodetectors exhibited impressive photoelectric performance at wavelengths of 475 nm and 532 nm. It demonstrated a high responsivity of 230.7 A/W, a remarkable specific detectivity of 1.794×10^{11} Jones, and a swift response speed of 60 ms at 475 nm. Furthermore, first-principles calculations based on density functional theory (DFT) were conducted to validate the oxidation kinetics of monolayer WS_2, the type II energy band alignment, and the interlayer charge transfer within the WSO_x/WS_2 vdWH. This research contributes novel insights into the synthesis of two-dimensional transition metal oxides (TMOs)-transition metal dichalcogenides (TMDCs) heterostructures for photodetector applications.

1. Introduction

Two-dimensional (2D) materials have garnered significant attention owing to their exceptional optoelectronic characteristics. In comparison to traditional semiconductor materials, 2D-based photodetectors exhibit a broad spectral response, remarkable stability, and substantial advantages in optoelectronic detection. These advantages stem from their tunable band gap ranging from 0 to 3 eV and their compact atomic and interlayer structure [1–5]. The advent of 2D transition metal dichalcogenides (TMDCs) has sparked immense research enthusiasm in the fields of nanoelectronics and optoelectronics. Characterized by unique physical attributes such as robust light-matter interactions, dangling-bond-free surfaces, and superior carrier mobility, 2D TMDCs serve as a versatile foundation for constructing heterojunctions. Leveraging the weak interlayer van der Waals forces, heterojunctions can be fabricated through layer-by-layer stacking of diverse 2D materials, regardless of their individual properties. This capability facilitates a diverse array of applications in optoelectronic devices, notably including photodetectors [6–12].

Atomic-thickness tungsten disulfide (WS_2), a member of the 2D TMDCs family, has garnered considerable attention for its application in photovoltaic devices such as photodetectors and photovoltaic cells. This is attributed to their high carrier mobility, exceptional thermal and chemical stability, and thickness-dependent bandgap, which have been extensively studied in literature [13–16]. The integration of WS_2 with various other 2D materials to form heterostructures opens up a broader horizon for the design and development of high-performance optoelectronic devices compared to using single WS_2 materials alone. Heterostructures provide a multitude of benefits, including enhanced functionality, a tunable band structure, improved carrier separation efficiency, and augmented light absorption capabilities [17,18]. These distinctive advantages position WS_2-based van der Waals heterojunctions (vdWHs) as promising candidates for optoelectronic detection applications and provide fertile ground for innovating and advancing

* Corresponding authors.
E-mail addresses: rjzhang@fudan.edu.cn (R. Zhang), hongyu_tang@fudan.edu.cn (H. Tang).

https://doi.org/10.1016/j.apsusc.2024.161848
Received 1 September 2024; Received in revised form 31 October 2024; Accepted 17 November 2024
Available online 19 November 2024

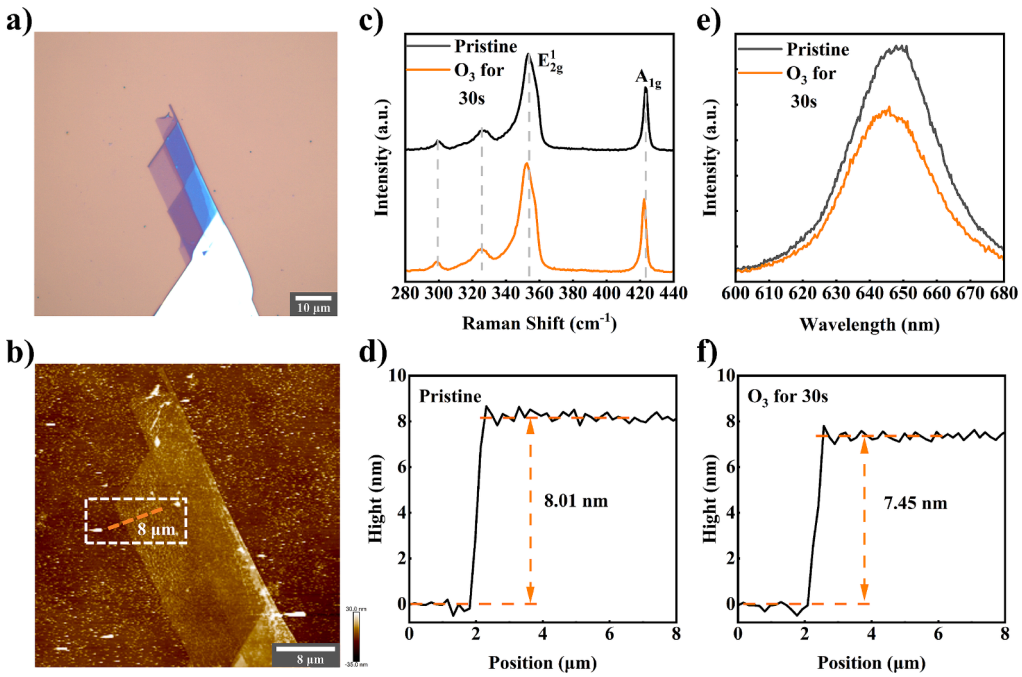

Fig. 1. a) Optical image of WS_2 film used for before and after-oxidation characterisation. b) AFM image of WS_2 thin films. c) Raman spectra of WS_2 and WSO_x/WS_2. d) WS_2 film thickness. e) PL spectra of WS_2 and WSO_x/WS_2. f) WSO_x film thickness.

high-performance optoelectronic devices.

To date, various WS_2-based 2D vdWHs have been fabricated for photodetector applications, encompassing combinations like WS_2/Bi_2Se_3 [19], $FePS_3/WS_2$ [20], and WS_2/GaAs [21], etc. Nonetheless, their use in devices also presents challenges due to their increased susceptibility to oxidation under ambient conditions [22]. In recent findings, Borah et al. leveraged oxidized WSe_2 to enhance the electrical properties of field-effect transistors (FETs) [23]. Similarly, Ngo et al. exhibited a technique for locally oxidizing WSe_2 FETs, yielding high-performance 2D p-type WSe_2 FETs [24]. Despite these advancements, the impact of oxidation on the optoelectronic performance of WS_2-based devices remains unexplored. Consequently, it is imperative to undertake a thorough examination of the oxidation mechanism of WS_2 and explore the preparation of 2D TMDCs heterojunction optoelectronic devices through controlled oxidation processes.

In this study, we report the fabrication of WSO_x/WS_2 heterojunction devices by transferring mechanically exfoliated WS_2 films onto SiO_2/Si substrates, followed by subsequent oxidation using ozone. These heterojunction devices exhibit exceptional photoresponse characteristics and robust stability. Notably, they demonstrate high responsivity (R_λ) values reaching 230.7 AW^{-1} and specific detectivity (D*) values as high as 1.794×10^{11} Jones. To gain deeper insights, we conducted first-principles calculations to investigate the electronic properties of both WS_2 and WSO_x/WS_2, including their adsorption and binding energies. Our findings reveal that the WSO_x/WS_2 heterojunction possesses a type-II band alignment, which is advantageous for enhancing photoelectric conversion efficiency, improving light absorption and emission performance, and promoting the effective separation of electrons and holes. Furthermore, we delved into the kinetics of WS_2 oxidation, aiming to provide a comprehensive mechanistic understanding and establish a foundational basis for the preparation of heterojunctions through controlled oxidation. Importantly, the devices demonstrate the capability for weak light detection at room temperature. The preparation method employed here is not only straightforward and controllable but also versatile, accommodating a wide range of TMDCs' oxidization.

2. Calculation method

All calculations in the CASTEP and Dmol3 modules are performed using first-principles density functional theory and Perdew Burke-Ernzerhof (PBE) pseudopotentials [25–27]. The Generalised Gradient Approximation (GGA) of the PBE was used for geometry optimization and energy band calculations with the truncation energy set to 450 eV [28,29]. The Monkhorst-Pack method was used to select a $12 \times 12 \times 1$ k-point grid in the Brillouin zone [30]. The thickness of the vacuum layer is set to 15 Å along the Z-axis to eliminate the interaction of periodic boundaries [31]. The results of vdW force interactions induced by weak interlayer coupling were corrected using the DFT-D3 method of Grimm [32]. The maximum displacement of each atom during structural relaxation was set to 0.2 μ m, and the convergence threshold of the atoms was set to 0.2 μ m. Energies and interatomic forces of 1×10^{-5} eV and 0.01 eV^{-1} were used for subsequent calculations of electronic properties. Calculations were performed with the Dmol3 code using the linear simultaneous and quadratic (LST/QST) method. Transition states and potential energies for O_3 dissociation and O atom substitution reactions were calculated using the LST/QST method, and transition states (TS) were obtained using the generalized LST/QST proposed by Govind from the original method of Halgren and Lipscomb [33,34].

3. Experimental section

3.1. Fabrication of WSO_x/WS_2 heterojunction devices

Thin WS_2 flakes were peeled from the bulk crystals by mechanical stripping using transparent adhesive tapes, and then the peeled WS_2 films were transferred to electrodes on SiO_2/Si substrates with pre-deposited electrodes (Ti/Au) using a PDMS-assisted dry transfer technique. The transferred films were then oxidized into an ozone environment at 100°C for 30 s and WSO_x was formed on the top layer of WS_2 to complete the preparation of WSO_x/WS_2 heterojunction devices. A small ozone generator provides ozone and maintains the ozone concentration in 0.0187 mg/L. Before transferring, the Si substrate was cleaned sequentially with ethanol and deionized water.

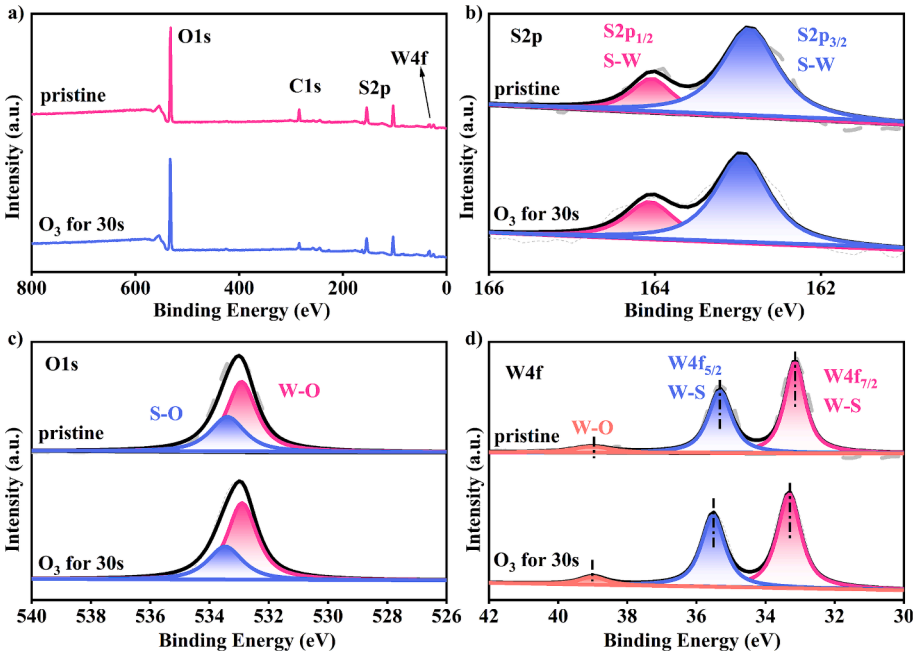

Fig. 2. XPS spectra for WS_2 and WSO_x/WS_2. a) Full − range XPS spectra, b) S 2p spectra, (c) O 1 s spectra, and (d) W 4f spectra.

3.2. Characterization

WS_2 films were imaged by a Keyence VHX-600 optical microscope. Raman spectra were obtained by confocal Raman microscopy system WITec alpha 300R (WITecInc., Germany) at room temperature (300 K) using 532 nm excitation. Morphological characterization was carried out using Bruker's Dimension Icon AFM model to measure the thickness of WS_2 before and after O_3 treatment, and the surface morphology and roughness of the samples were analyzed using Nanoscope Analysis software to obtain the thickness of the test samples. Chemical compositions and element ratios were examined using X-ray photoelectron spectroscopy (XPS; Thermo Scientific K-Alpha +). We conducted all I-V curve measurements in a probe station using a digital source meter (Keithley 2636). To provide illumination, a 150 W-Xe lamp (Zolix Gloria-X150A) served as the light source, while a monochromator (Zolix omni-3047i) enabled the selection of specific wavelengths and spectral scanning. Light-path on/off was managed by a mechanical shutter controlled through a repeated transistor-transistor logic (TTL) signal. For calibration purposes, we utilized the opto-electrical response of a standard Si detector (Hamamatsu, QE-B3-UV) as a reference.

4. Results and discussions

The WS_2 thin film and WSO_x/WS_2 heterojunction are characterized by means of AFM, optical spectroscopy techniques and XPS. Fig. 1a illustrates the structure diagram of the WS_2 thin film on SiO_2/Si substrate. The WSO_x/WS_2 heterojunction is prepared by dry transferring of WS_2 thin film with subsequent ozone oxidation method as has described in the experiment. AFM image for characterizing the morphology and structure of the WS_2 thin film and WSO_x/WS_2 heterojunction is shown in Fig. 1b. Raman spectra are employed to further investigate the crystalline structures and qualities of the mechanically exfoliated WS_2 and

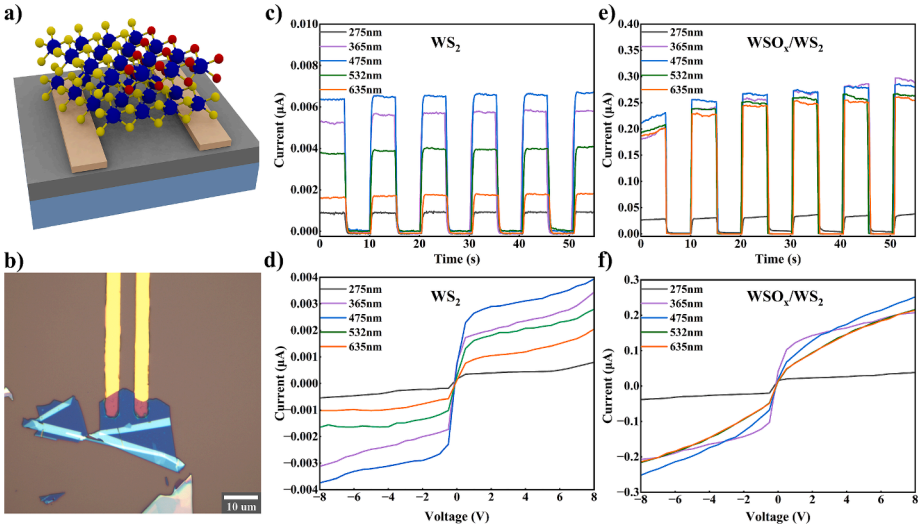

Fig. 3. a) Schematic of the heterojunction device. b) Optical image of the WSO_x/WS_2 photodetector. c,d) I-t curves of pristine WS_2 and WSO_x/WS_2 photodetectors irradiated at V_{ds} = +5 V and 18.2 μW· cm^{-2} power density of 275 nm, 365 nm, 475 nm, 532 nm and 635 nm lasers. e,f) I-V curves of pristine WS_2 and WSO_x/WS_2 photodetectors irradiated by lasers of different wavelengths.

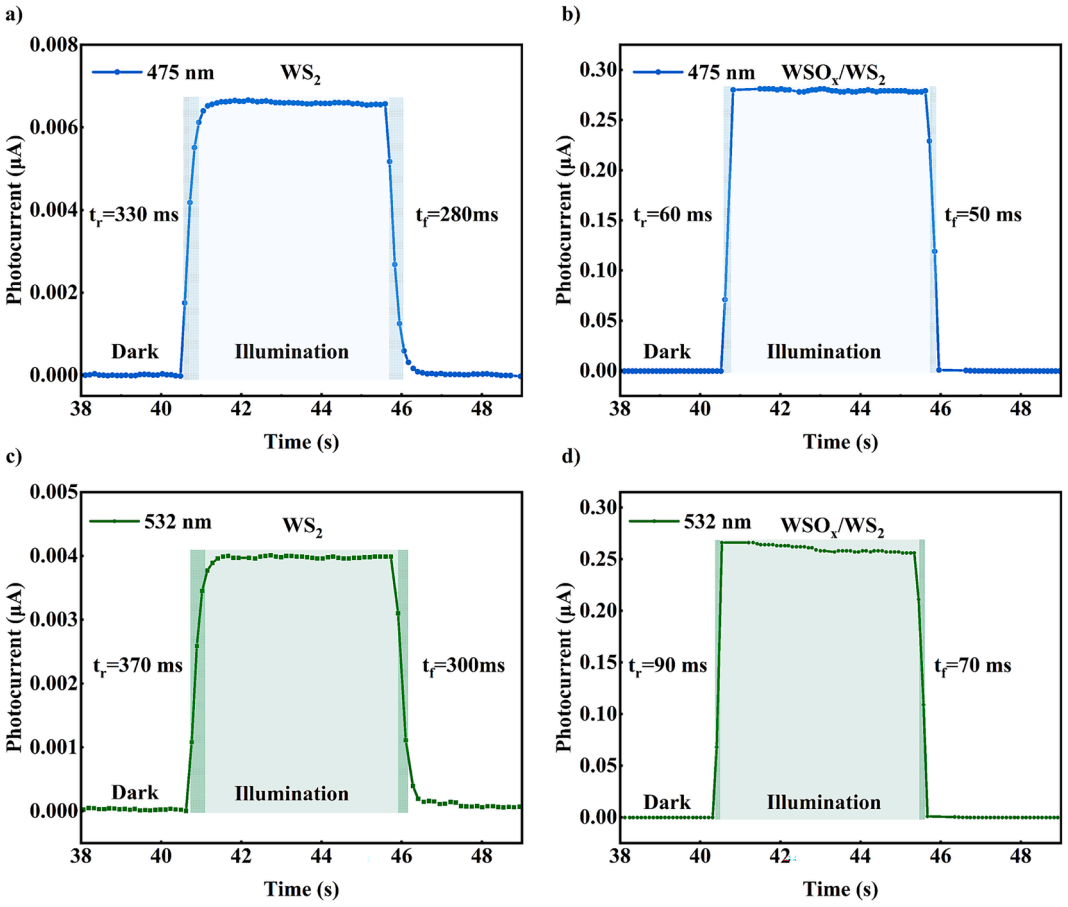

Fig. 4. Dynamic photoresponse of a) WS_2 and b) WSO_x/WS_2 devices under 475 nm light irradiation, Dynamic photoresponse of a) WS_2 and b) WSO_x/WS_2 devices under 532 nm light irradiation.

WSO_x/WS_2 heterojunction. Fig. 1c shows the Raman spectra of WS_2 and WSO_x/WS_2 heterojunction at room temperature with laser excitation at 532 nm. The observed Raman characteristic peaks of WS_2 are located at 352.5 and 421.5 cm^{-1} corresponding to the in-plane vibration E^1_{2g} mode and the out-of-plane A_{1g} mode, respectively [35]. Compared with WS_2, the peaks of the E^1_{2g} and A_{1g} of WSO_x/WS_2 heterojunction have a relative blue-shift of $\Delta\omega$ of 1.02 and 1.31 cm^{-1}, respectively, while the remaining peaks are not shifted. The changes in vibrational modes indicate that there is a strong interlayer coupling between the WS_2 and WSO_x/WS_2 heterojunction. PL spectra of WS_2 and WSO_x/WS_2 heterostructure are shown in Fig. 1e. It indicates that the PL peak intensity of the WSO_x/WS_2 heterojunction is weaker than that of WS_2 significantly. This quenching phenomenon effectively proves the charge separation at the heterojunction, further verifies the interlayer coupling effect in the heterostructure, and indicates the photoexcited charge carriers undergo non-radiation recombination instead of PL emission [36]. It implies that an ultrafast photoexcited carrier transportation will occur at the interface of the heterostructure. In Fig. 1d and f, the thicknesses of WS_2 and WSO_x/WS_2 are 8.01 and 7.45 nm, respectively. The results show that O atoms substitution occurs in the top layer of the WS_2 film by oxidation, which leads to a reduction in the thickness of the WS_2 layer.

XPS was conducted to further confirm the elemental composition and bonding state of the WSO_x/WS_2 heterostructure. In Fig. 2a, the XPS spectrum clearly shows W, S, and O elements after C1s spectrum calibration. The S 2p spectra of these composites were characterized in Fig. 2b. Fig. 2c shows that the O 1 s spectra of the WSO_x/WS_2 heterostructure can be well fitted into the peak at 530.40 eV. Fig. 2d displays the W4f spectra of WS_2 and WSO_x/WS_2. The two peaks of W $4f_{5/2}$ and W $4f_{7/2}$ of WS_2 are situated at about 33.24 eV and 35.4 eV. After oxidation, compared with WS_2, the peak of W $4f_{5/2}$ and the W-O band of WSO_x/WS_2 heterojunction exhibit displacement to higher energy, while the remaining peaks maintain their original position. It is conceivable that the O elements may be responsible for the transfer of electrons, thereby enabling W to attain a greater degree of binding energy, a result consistent with previous reports [37,38]. Summarily, all the XPS spectra results imply the WS_2 thin film is oxidized and demonstrates a successful construction of WSO_x/WS_2 heterostructure.

Fig. 3a illustrates the structure diagram of the WSO_x/WS_2 vdWH photodetector constructed on SiO_2/Si substrate. The optical image of the device is shown in Fig. 3b. Fig. 3c-f present the switching behavior of the devices under periodic illumination with different wavelengths from UV to VIS (Ultraviolet to Visible light, including 275, 365, 475, 532 and 635 nm), with a power intensity of 18.2 μW at $V_{ds} = +5$ V. Compared with WS_2 photodetector, the photoelectric response capability of WSO_x/WS_2 heterojunction photodetector enhances about 45 times. Fig. 3e and d show the output characteristic curves (I_{ds}-V_{ds}) of the devices with 275, 365, 475, 532 and 635 nm laser irradiations. The findings demonstrate that the higher photocurrent is generated by 475 nm laser irradiation of both WS_2 and WSO_x/WS_2 heterojunction photodetectors than that of other light wavelengths. Additionally, the photocurrent of WSO_x/WS_2 is observed to be approximately 64 times higher than that of WS_2. In general, at all illumination wavelengths above, the WSO_x/WS_2 heterojunction device yields a definite switching behavior and exhibits superior photoelectric performance than the WS_2 device, demonstrating its feasibility for stable photodetection.

Response time describes the instantaneous response speed of the photodetector to the change of the input optical signal and records the transient photocurrent signal of the device. As illustrated in Fig. 4, we

Table 1
Performance comparison of various photodetectors based on 2D TMDCs.

Devices	Wavelength [nm]	Response time [τr/τf ms]	Responsivity [AW^{-1}]	D* [Jones]	Photocurrent I_{ph} (μA)	Ref.
WO_3	382	530/530	1.002	–	18.05	[43]
GaSe/ReS_2	340 nm	261/274	170	–	20.71	[44]
WS_2/WO_3	382/512	100/100	2.94/2.02	$14.19/9.71 \times 10^{10}$	486.43/292.81	[45]
	458–647	5.3/5.3	9.27×10^{-5}	4.7×10^{5}	–	[46]
WS_2						
MoS_2/WS_2	532	80/60	1.1×10^{-3}	2.5×10^{6}	–	[47]
WSO_x/WS_2	475–635	70/60	230.7	1.794×10^{11}	0.252	this work

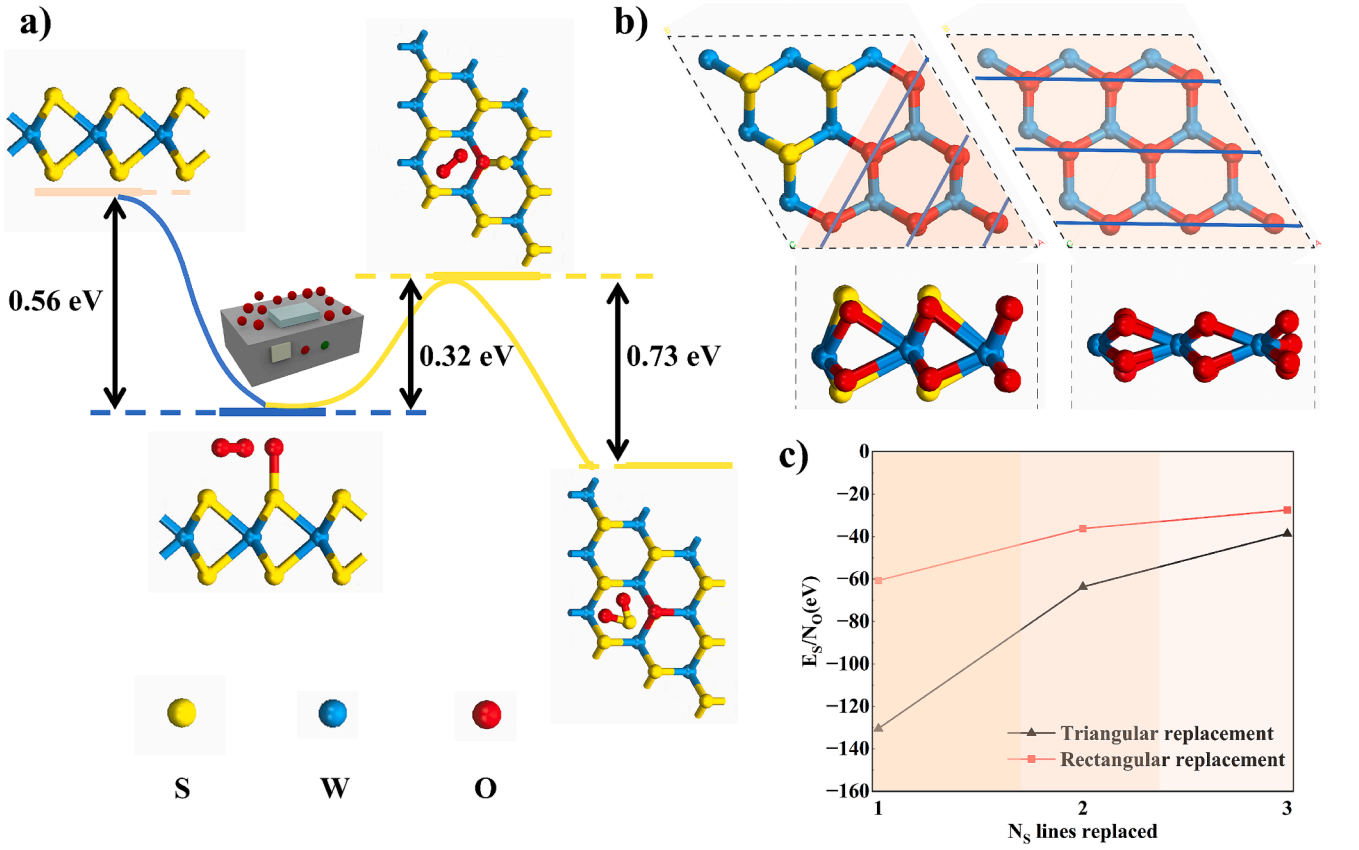

Fig. 5. Reaction kinetics of the oxidized structure of WS_2. a) Reaction kinetics and transition states during oxidation. b) Triangular O-substituted structure of a 3x3 monolayer WS_2 supercell; Rectangular O-substituted structure of a 3x3 monolayer WS_2 supercell. c) Stability energies (E_S) normalized to the number of substituting O atoms (N_O) as a function of the number of S-lines with triangular (delta) and rectangular (square) substitutions. As a function of the number of O atoms substituted from spectral line 1 to spectral line 3.

have measured the photoswitching characteristics of both WS_2 and WSO_x/WS_2 devices at wavelengths of 475 nm and 532 nm, respectively. Specifically, the rise time and fall time are defined as the durations required for the photocurrent to transition from 10 % to 90 % and from 90 % to 10 % of the stable photocurrent value, respectively, serving as indicators of the device's sensitivity [39]. From the I-t curves of the devices, it is apparent that the WSO_x/WS_2 heterojunction device demonstrates swift rise and fall times of 60 ms and 50 ms at 475 nm, and 90 ms and 70 ms at 532 nm. These times are more than an order of magnitude faster compared to the WS_2 device under laser illumination at 475 nm.

Furthermore, the key performance parameters of photoresponsivity (R_λ) and specific detectivity (D*) are evaluated by the following equations [40,41]:

$$R\lambda = \frac{(I_{photo} - I_{dark})}{P \cdot S} \quad (1)$$

$$D^* = \frac{R_\lambda \cdot \sqrt{S}}{\sqrt{2eI_{dark}}} \quad (2)$$

where I_{photo} and I_{dark} are the photocurrent and dark current, respectively, P is the laser power density, S is the effective area upon illumination (60 μm^2), e is the electronic charge. In this work, R_λ and D* at the illumination power density of 18.2 $\mu W/mm^{-2}$ are calculated to be 230.7 A W^{-1} and 1.794×10^{11} Jones, respectively. The R_λ can intuitively reflect the sensitivity of the devices [42]. Table 1 summarizes the important figures-of-merit of the previous reports. Generally, our device stands out considering the detectivity and response time.

To achieve a better understanding of oxidation mechanism of monolayer WS_2, the oxidation process of monolayer WS_2 is studied by DFT calculation. The energy barriers and transition states during the oxidation of WS_2 are investigated by first-principles calculations. Fig. 5a shows the formation of O_3 dissociation, O atom adsorption to form S-O bonds, and O atom substitution during the reaction of O_3 with WS_2. To

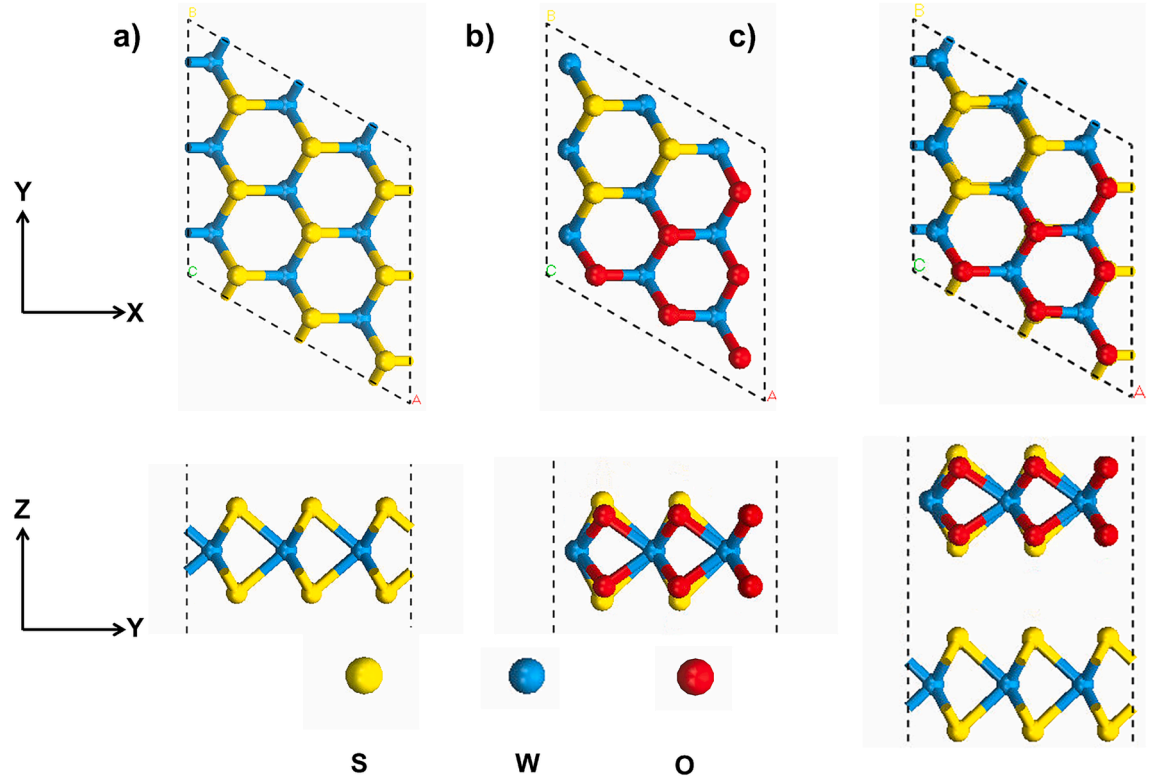

Fig. 6. Top and side views of the optimized structure. a) 3x3 monolayer WS_2 supercell. b) Top and side views of 3x3 monolayer WSO_x supercell. c) Top and side views of WSO_x/WS_2 heterostructure.

determine the energies of the transition states and to find the energy barriers for the oxidation substitution process, we used the calculation method of the Climbing Image Nudge Elastic Band (CI-NEB) model [34]. The results show that the energy barrier of our proposed reaction pathway is 0.32 eV after the adsorption reaction with oxygen atoms on the surface of WS_2 crystals, and the energy enthalpy of this reaction changes to −0.41 eV, which implies that the substitution of oxygen atoms by sulfur atoms after the dissociation of O_3 molecules is thermodynamically favorable.

In addition, we investigated the adsorption energy of ozone with the monolayer WS_2 surface, and the equation for the enthalpy change of adsorption energy was defined as:

$$E_{(adsorption)} = E_{(WS2)} + E_{(O3)} - E_{(WS2+O3)} = -0.49eV \quad (3)$$

Calculations show that the reaction of ozone adsorption on a monolayer WS_2 surface is also thermodynamically favorable [48–50]. To determine the oxidation structure of WS_2, as shown in Fig. 5b, the O atom spectral lines were used to gradually replace the S atom spectral lines, forming triangular and rectangular structures, respectively. The stability energies of the oxidation structure of WS_2 are defined as:

$$E_S = E_{Total} - \sum_i N_i E_i \quad (4)$$

where E_S is the stabilization energy and E_{Total} is the total energy of the system, obtained from the Dmol3 calculation module. N_i and E_i are the number and energy of individual atoms of species i (i = W, S, O), respectively [51,52]. The results in Fig. 5c show that the stability of the structure substituted with triangular oxide islands is higher than that of the structure with rectangular oxide islands. Therefore, we determined the structure of WS_2 oxidation by calculating the stability energy, and this result is consistent with the oxidation structures of other TMDCs materials [53,54].

For further investigating the electronic properties of WSO_x/WS_2 vdWH the band structure, and partial-wave density of states (PDOS) of

Table 2
Specific parameters of WS_2, WSOx, and the $WSOx/WS_2$ heterojunction.

System	$L_{W\text{-}S}$(Å)	$L_{W\text{-}O}$(Å)	d(Å)	E_b(eV)
WS_2	2.416			
WSOx	2.416	2.037		
$WSOx/WS_2$	2.443	2.068	3.255	−5.133

WSO_x/WS_2 vdWH, monolayer WSO_x and monolayer WS_2 were computed by PBE method. The lattice parameters of the WSO_x monolayer and WS_2 monolayer are 3.76 Å and 3.52 Å, respectively. The monolayer WSO_x and monolayer WS_2 were expanded by 3 × 3 × 1, respectively, and the optimized WSO_x was vertically stacked on top of the optimized WS_2 to construct a vdWH. Fig. 6a-c depict the top and side views of the optimized WS_2 monolayer, WSO_x monolayer, and WSO_x/WS_2 vdWH, respectively. To investigate the stability of the WSO_x/WS_2 vdWH structure, the binding energy (E_b) of the WSO_x/WS_2 vdWH was calculated. The calculation formula is given below:

$$E_b = E_{WSOx/WS2} - E_{WSOx} - E_{WS2} \quad (5)$$

where $E_{WSOx/WS2}$ is the energy of the WSO_x/WS_2 vdWH, E_{WSOx} is the energy of the monolayer WSO_x, and E_{WS2} is the energy of the monolayer WS_2. The smaller the E_b (the larger the negative value), the more stable the structure [55]. The calculated E_b of the WSO_x/WS_2 vdWH is −5.133 eV, thus, the WSO_x/WS_2 vdWH of the above configuration is a stable structure, and the specific parameters of the WSO_x/WS_2 vdWH are shown in Table 2.

As demonstrated in Fig. 7a monolayer WS_2 has a direct band gap with 1.865 eV, both the valence-band maximum (VBM) and the conduction band minimum (CBM) located at Γ. From the PDOS diagram of the WS_2 monolayer, it can be perceived that CBM is chiefly rendered over *d* and *p* orbitals of the W. VBM is chiefly afforded via *p* orbitals of

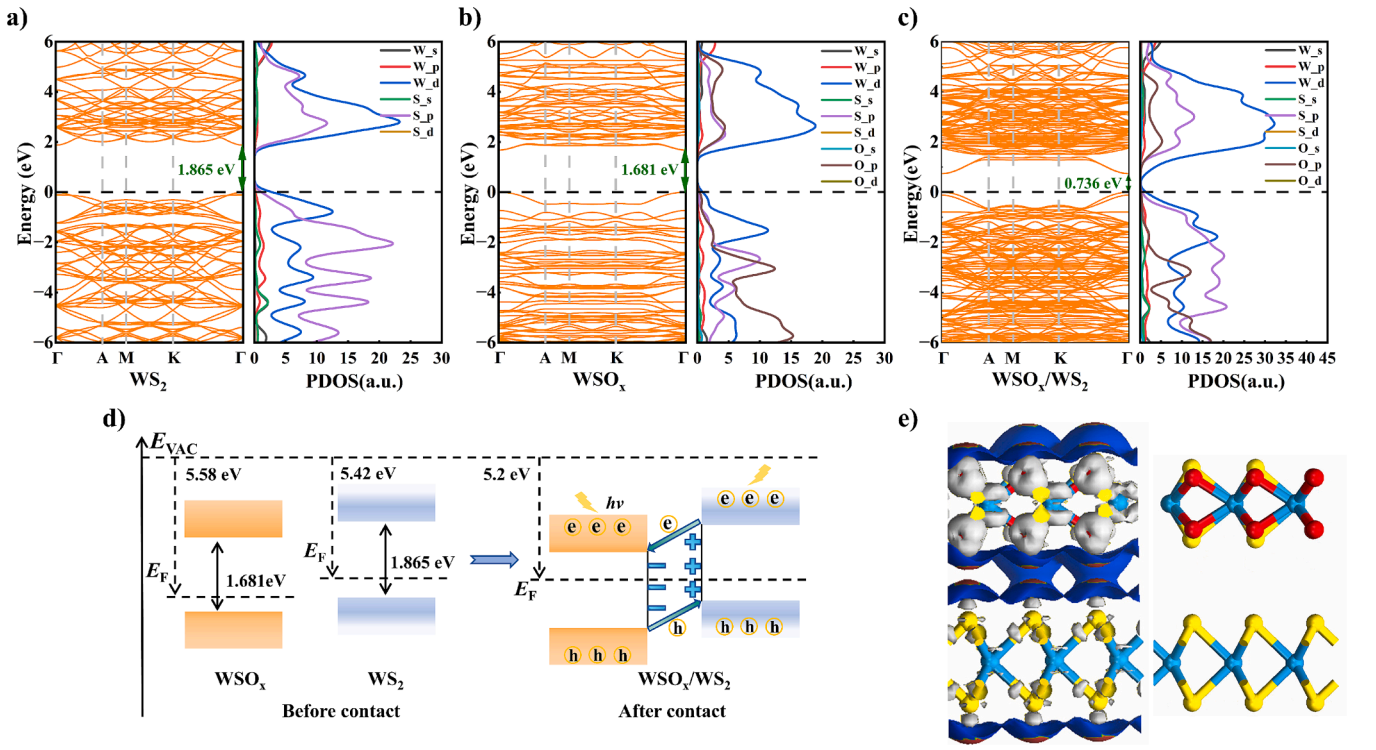

Fig. 7. a) Energy band structure and PDOS plots of monolayer WS_2 supercells. b) Energy band structure and PDOS plots of monolayer WSO_x supercells. c) Energy band structure and PDOS plots of WSO_x/WS_2 heterojunction supercells. d) Alignment of type II energy bands of WSO_x/WS_2 heterostructures. e) Difference in charge densities of WSO_x/WS_2 heterostructures.

the S. As showcased in Fig. 7b monolayer WSO_x has a direct band gap with 1.681 eV. CBM is basically afforded over *d* orbital of W, while VBM is chiefly rendered via *d* and *p* orbitals of O. As showcased in Fig. 7c WSO_x/WS_2 vdWH has a direct band gap of 0.736 eV, which is much smaller than two monolayers, and more favourable for the excitation of photogenerated electrons.

As a key parameter, the work function is calculated as follows:

$$W = E_{VAC} - E_F \tag{6}$$

where E_{VAC} represents the energy level of stationary electrons in vacuum and E_F represents the Fermi level [56]. The calculated work functions of the WSO_x and WS_2 monolayers are 5.58 eV and 5.42 eV, separately. The work function of the WSO_x/WS_2 vdWH is 5.2 eV. As shown in Fig. 7d, the band alignment of WSO_x monolayer, WS_2 monolayer, and WSO_x/WS_2 vdWH. Since the Fermi energy (E_F) of the WSO_x layer is smaller than that of the WS_2 layer, when the two layers contact, electrons will run from the conduction band of the WS_2 to the conduction band of the WSO_x, and holes will run from the valence band of the WSO_x to the valence band of the WS_2 [57]. When carriers diffuse, the E_F of WS_2 decreases, while the E_F of WSO_x rises eventually reaching equilibrium.

As an important model to study the properties of atoms and molecules and its interactions [58], the charge density difference can be used to gain a better understanding of charge transfer in heterostructures at the interface using the form $\Delta\rho = \rho_{WSOx/WS2} - \rho_{WSOx} - \rho_{WS2}$, where $\rho_{WSOx/WS2}$, ρ_{WSOx}, and ρ_{WS2} represent the charge densities of the heterostructure, WSO_x, and WS_2 structures, respectively. Fig. 7e illustrates the differential charge density of WSO_x/WS_2 heterostructures. We can find that there is charge accumulation at the interface area of WSO_x and WS_2. The blue isosurface represents the negative charge accumulation region and yellow represents the positive charge depletion region, respectively. Combining the analysis of the differential charge density and band structure, we find that WSO_x has a moderating effect on the electronic structure of WS_2 and facilitating the generation and separation of electron-hole pairs [59,60]. Consequently, the WSO_x/WS_2 vdWH device has a faster response as well as a higher responsivity than that of WS_2 device.

5. Conclusions

In conclusion, we introduce a straightforward method for synthesizing WSO_x/WS_2 vertical vdWHs by oxidizing the top layer of WS_2 to form a WSO_x layer through O_3 oxidation at an ambient temperature of 100 °C. The thickness and structure of the heterojunction are characterized using AFM, Raman and PL spectroscopy, and XPS, respectively. The results confirm the successful synthesis of WSO_x/WS_2 heterojunctions. Compared to the WS_2 device, the WSO_x/WS_2 vdWH device exhibits superior photoelectric performance, including a high responsivity of 230.7 A/W, and a promising and reliable detectivity of 1.794×10^{11} Jones, a higher photocurrent of 0.252 μA, and a faster photoelectric response time of approximately 60 ms at 475 nm. Regarding the mechanism anlaysis, we present the thermodynamic energy barriers, transition states, and oxidation structure of monolayer WS_2 during the oxidation process through DFT calculations. It is found that the heterojunction forms a type II energy band structure, which facilitates the effective separation of photogenerated electron-hole pairs. This, in turn, enhances the photocurrent and responsivity of the WSO_x/WS_2 heterojunction devices. Notably, the devices are capable of detecting weak light at room temperature. More importantly, the preparation method is straightforward and controllable, accommodating a wide range of TMDCs' oxidization. This study provides a viable route and theoretical foundation for the synthesis of transition-metal oxides (TMOs)-TMDCs heterostructures for applications in photodetectors.

CRediT authorship contribution statement

Weiqi shi: Writing – original draft, Visualization, Software, Methodology, Formal analysis, Data curation, Conceptualization. **Yifang Ding:** Validation, Investigation. **Shaojun Fang:** Investigation, Data

curation. **Hong Zhou:** Visualization, Validation, Methodology. **Jiao Qi:** Methodology, Investigation, Formal analysis. **Jiajie Fan:** Supervision, Writing – review & editing. **Rongjun Zhang:** Writing – review & editing, Supervision, Conceptualization. **Guoqi Zhang:** Visualization, Supervision. **Hongyu Tang:** Writing – review & editing, Supervision, Investigation, Funding acquisition, Conceptualization.

Declaration of competing interest

The authors declare that they have no known competing financial interests or personal relationships that could have appeared to influence the work reported in this paper.

Acknowledgments

This study was supported by Shanghai Research Center for Silicon Carbide Power Devices Engineering & Technology Project [Grant No. 19DZ2253400] and National Natural Science Foundation of China [Grant No. U2230108].

Data availability

Data will be made available on request.

References

[1] X.Y. Chen, C.B. Liu, S. Mao, Environmental Analysis with 2D Transition-Metal Dichalcogenide-Based Field-Effect Transistors, Nano-Micro Lett. 12 (1), 24 (2020) Review.
[2] L. Jiang, S.W. Zeng, Q.L. Ouyang, X.Q. Dinh, P. Coquet, J.L. Qu, S.L. He, K.T. Yong, Graphene-TMDC-Graphene Hybrid Plasmonic Metasurface for Enhanced Biosensing: A Theoretical Analysis, Phys. Status Solidi A-Appl. Mat. 214 (12) (2017) 11.
[3] T.H. Ren, K.P. Loh, On-chip integrated photonic circuits based on two-dimensional materials and hexagonal boron nitride as the optical confinement layer, J. Appl. Phys. 125 (23) (2019) 13.
[4] Y. Xiao, M.Y. Zhou, M.Q. Zeng, L. Fu, Atomic-Scale Structural Modification of 2D Materials, Adv. Sci. 6 (5) (2019) 15.
[5] J.X. Yan, K. Ye, Z.Y. Jia, Z.Y. Zhang, P.H. Li, L.X. Liu, C.P. Mu, H. Huang, Y. C. Cheng, A.M. Nie, et al., High-Performance Broadband Image Sensing Photodetector Based on MnTe/WS2van der Waals Epitaxial Heterostructures, ACS Appl. Mater. Interfaces 16 (15) (2024) 19112–19120.
[6] W. Ahmad, J. Wu, Q.D. Zhuang, A. Neogi, Z.M. Wang, Research Process on Photodetectors based on Group-10 Transition Metal Dichalcogenides, Small 19 (16) (2023) 32.
[7] Choi, W.; Choudhary, N.; Han, G. H.; Park, J.; Akinwande, D.; Lee, Y. H. Recent development of two-dimensional transition metal dichalcogenides and their applications. *Materials Today* **2017**, *20* (3), 116-130, Review.
[8] Duan, X. D.; Wang, C.; Pan, A. L.; Yu, R. Q.; Duan, X. F. Two-dimensional transition metal dichalcogenides as atomically thin semiconductors: opportunities and challenges. *Chem. Soc. Rev.* **2015**, *44* (24), 8859-8876, Review.
[9] Huang, Y.; Pan, Y. H.; Yang, R.; Bao, L. H.; Meng, L.; Luo, H. L.; Cai, Y. Q.; Liu, G. D.; Zhao, W. J.; Zhou, Z.; et al. Universal mechanical exfoliation of large-area 2D crystals (vol 11, 2453, 2020). *Nat. Commun.* **2020**, *11* (1), 1, Correction.
[10] A.G. Rajan, V. Sresht, A.A.H. Padua, M.S. Strano, D. Blankschtein, Dominance of Dispersion Interactions and Entropy over Electrostatics in Determining the Wettability and Friction of Two-Dimensional MoS2 Surfaces, ACS Nano 10 (10) (2016) 9145–9155.
[11] A. Weston, Y.C. Zou, V. Enaldiev, A. Summerfield, N. Clark, V. Zolyomi, A. Graham, C. Yelgel, S. Magorrian, M.W. Zhou, et al., Atomic reconstruction in twisted bilayers of transition metal dichalcogenides, Nat. Nanotechnol. 15 (7) (2020) 592.
[12] Xu, H.; Ding, Z. J.; Nai, C. T.; Bao, Y.; Cheng, F.; Tan, S. J. R.; Loh, K. P. Controllable Synthesis of 2D and 1D MoS2 Nanostructures on Au Surface. *Adv. Funct. Mater.* **2017**, *27* (19), 8, ; Proceedings Paper.
[13] R.B. Jacobs-Gedrim, M. Shanmugam, N. Jain, C.A. Durcan, M.T. Murphy, T. M. Murray, R.J. Matyi, R.L. Moore, B. Yu, Extraordinary Photoresponse in Two-Dimensional In2Se3 Nanosheets, ACS Nano 8 (1) (2014) 514–521.
[14] N. Perea-López, A.L. Elías, A. Berkdemir, A. Castro-Beltran, H.R. Gutiérrez, S. M. Feng, R.T. Lv, T. Hayashi, F. López-Urías, S. Ghosh, et al., Photosensor Device Based on Few-Layered WS2 Films, Adv. Funct. Mater. 23 (44) (2013) 5511–5517.
[15] H.J. Tan, W.S. Xu, Y.W. Sheng, C.S. Lau, Y. Fan, Q. Chen, M. Tweedie, X.C. Wang, Y.Q. Zhou, J.H. Warner, Lateral Graphene-Contacted Vertically Stacked WS2/MoS2 Hybrid Photodetectors with Large Gain, Adv. Mater. 29 (46) (2017) 8.
[16] Y.Z. Xue, Y.P. Zhang, Y. Liu, H.T. Liu, J.C. Song, J. Sophia, J.Y. Liu, Z.Q. Xu, Q. Y. Xu, Z.Y. Wang, et al., Scalable Production of a Few-Layer MoS2/WS2 Vertical Heterojunction Array and Its Application for Photodetectors, ACS Nano 10 (1) (2016) 573–580.
[17] Y. Liu, N.O. Weiss, X.D. Duan, H.C. Cheng, Y. Huang, X.F. Duan, Van der Waals heterostructures and devices, Nat. Rev. Mater. 1 (9) (2016) 17.
[18] Xia, F. N.; Wang, H.; Xiao, D.; Dubey, M.; Ramasubramaniam, A. Two-dimensional material nanophotonics. *Nat. Photonics* **2014**, *8* (12), 899-907, Review.
[19] F. Li, J.L. Li, J.S. Zheng, Y.B. Tong, H.F. Zhu, P. Wang, L.J. Li, Fast Fabrication of WS2/Bi2Se3 Heterostructures for High-Performance Photodetection, ACS Appl. Mater. Interfaces 15 (7) (2023) 10098–10108.
[20] X.Y. Cao, S.H. Yan, Z.T. Li, Z.H. Fang, L. Wang, X.F. Liu, Z.W. Chen, H.C. Lei, X. Zhang, Broadband Photodetector Based on FePS3/WS2 van der Waals Type II Heterostructure, J. Phys. Chem. Lett. 14 (50) (2023) 11529–11535.
[21] K.L. Li, W.J. Wang, J.F. Li, W.X. Jiang, M. Feng, Y. He, High-responsivity, self-driven photodetectors based on monolayer WS2/GaAs heterojunction, Photonics Res. 8 (8) (2020) 1368–1374.
[22] M. Buscema, J.O. Island, D.J. Groenendijk, S.I. Blanter, G.A. Steele, H.S.J. van der Zant, A. Castellanos-Gomez, Photocurrent generation with two-dimensional van der Waals semiconductors, Chem. Soc. Rev. 44 (11) (2015) 3691–3718.
[23] A. Borah, A. Nipane, M.S. Choi, J. Hone, J.T. Teherani, Low-Resistance p-Type Ohmic Contacts to Ultrathin WSe2 by Using a Monolayer Dopant, ACS Appl. Electron. Mater. 3 (7) (2021) 2941–2947.
[24] T.D. Ngo, T. Huynh, I. Moon, T. Taniguchi, K. Watanabe, M.S. Choi, W.J. Yoo, Self-Aligned Top-Gate Structure in High-Performance 2D p-FETs via van der Waals Integration and Contact Spacer Doping, Nano Lett. 23 (23) (2023) 11345–11352.
[25] G. Kresse, J. Furthmuller, Efficient iterative schemes for ab initio total-energy calculations using a plane-wave basis set, Phys. Rev. B 54 (16) (1996) 11169–11186.
[26] H. Orita, N. Itoh, Y. Inada, All electron scalar relativistic calculations on adsorption of CO on Pt(111) with full-geometry optimization: a correct estimation for CO site-preference, Chem. Phys. Lett. 384 (4–6) (2004) 271–276.
[27] R.C. Peng, W. Zeng, Q. Zhou, Adsorption and gas sensing of dissolved gases in transformer oil onto Ru3-modified SnS2: A DFT study, Appl. Surf. Sci. 615 (2023) 9.
[28] T. Bucko, J. Hafner, S. Lebègue, J.G. Angyán, Improved Description of the Structure of Molecular and Layered Crystals: Ab Initio DFT Calculations with van der Waals Corrections, J. Phys. Chem. A 114 (43) (2010) 11814–11824.
[29] J.P. Perdew, K. Burke, M. Ernzerhof, Generalized gradient approximation made simple, Phys. Rev. Lett. 77 (18) (1996) 3865–3868.
[30] Pack, J. D.; Monkhorst, H. J. SPECIAL POINTS FOR BRILLOUIN-ZONE INTEGRATIONS - REPLY. *Phys. Rev. B* **1977**, *16* (4), 1748-1749, Letter.
[31] Z. Wang, Y. Zhang, X. Wei, T.T. Guo, J.B. Fan, L. Ni, Y.J. Weng, Z.D. Zha, J. Liu, Y. Tian, et al., Type-II tunable SiC/InSe heterostructures under an electric field and biaxial strain, Phys. Chem. Chem. Phys. 22 (17) (2020) 9647–9655.
[32] S. Grimme, Semiempirical GGA-type density functional constructed with a long-range dispersion correction, J. Comput. Chem. 27 (15) (2006) 1787–1799.
[33] Govind, N.; Petersen, M.; Fitzgerald, G.; King-Smith, D.; Andzelm, J. A generalized synchronous transit method for transition state location. *Comput. Mater. Sci.* **2003**, *28* (2), 250-258, Proceedings Paper.
[34] T.A. Halgren, W.N. Lipscomb, SYNCHRONOUS-TRANSIT METHOD FOR DETERMINING REACTION PATHWAYS AND LOCATING MOLECULAR TRANSITION-STATES, Chem. Phys. Lett. 49 (2) (1977) 225–232.
[35] A. Berkdemir, H.R. Gutiérrez, A.R. Botello-Méndez, N. Perea-López, A.L. Elías, C. I. Chia, B. Wang, V.H. Crespi, F. López-Urías, J.C. Charlier, et al., Identification of individual and few layers of WS2 using Raman Spectroscopy, Sci Rep 3 (2013) 8.
[36] X.Y. Wang, L. Tong, W.H. Fan, W. Yan, C. Su, D.J. Wang, Q.G. Wang, H. Yan, S. G. Yin, Air-stable self-powered photodetector based on TaSe2/WS2/TaSe2 asymmetric heterojunction with surface self-passivation, Journal of Colloid and Interface Science 657 (2024) 529–537.
[37] G.P. Li, Y.L. Wang, J.T. Bi, X. Huang, Y.F. Mao, L. Luo, H. Hao, X. Partial Oxidation Strategy to Synthesize WS2/WO3 Heterostructure with Enhanced Adsorption Performance for Organic Dyes: Synthesis, Modelling, and Mechanism. Nanomaterials 10 (2) (2020).
[38] Z. Masoumi, M. Tayebi, M. Kolaei, B.K. Lee, Efficient and stable core-shell ?-Fe2O3/WS2/WOx photoanode for oxygen evolution reaction to enhance photoelectrochemical water splitting, Applied Catalysis B-Environmental 313 (2022).
[39] X. Zhou, X.Z. Hu, S.S. Zhou, H.Y. Song, Q. Zhang, L.J. Pi, L. Li, H.Q. Li, J.T. Lü, T. Y. Zhai, Tunneling Diode Based on WSe2/SnS2 Heterostructure Incorporating High Detectivity and Responsivity, Adv. Mater. 30 (7) (2018) 8.
[40] B. Yan, B. Ning, G.X. Zhang, D.H. Zhou, X. Shi, C.X. Wang, H.Q. Zhao, Ultra-Thin GeSe/WS2 Vertical Heterojunction with Excellent Optoelectronic Performances, Adv. Opt. Mater. 10 (6) (2022).
[41] S. Feng, C. Liu, Q.B. Zhu, X. Su, W.W. Qian, Y. Sun, C.X. Wang, B. Li, M.L. Chen, L. Chen, et al., An ultrasensitive molybdenum-based double-heterojunction phototransistor, Nat. Commun. 12 (1) (2021).
[42] M. Liao, Progress in semiconductor diamond photodetectors and MEMS sensors, Functional Diamond 1 (1) (2022) 29–46.
[43] P.K. Yadav, Y. Ashok Kumar Reddy, B. Ajitha, Vasudeva Reddy, Minnam Reddy, Oxygen partial pressure dependent UV photodetector performance of WO3 sputtered thin films, J. Alloy. Compd. 816 (2020) 152565.
[44] M. Mahajan, S. Kallatt, M. Dandu, N. Sharma, S. Gupta, K. Majumdar, Light emission from the layered metal 2H-TaSe2 and its potential applications, Commun. Phys. 2 (2019) 88.
[45] P.V.K. Yadav, Y.A.K. Reddy, WS2/WO3 Heterostructure-Based Photodetectors on SiO2/Si for Future Optoelectronics, ACS Appl. Electron. Mater. 5 (5) (2023) 2538–2547.

[46] N. Perea López, A. L. Elías, A. Berkdemir, A. Castro Beltran, H. R. Gutiérrez, S. Feng, R. Lv, T. Hayashi,F. López Urías, S. Ghosh, B. Muchharla, S. Talapatra, H. Terrones and M. Terrones, Adv. Funct. Mater., 2013, 23, 5511–5517.
[47] C. Chen, Y. Yang, X. Zhou, W.X. Xu, Q.N. Cui, J.B. Lu, H.M. Jing, D. Tian, C.X. Xu, T.Y. Zhai, et al., Synthesis of Large-Area Uniform MoS2-WS2 Lateral Heterojunction Nanosheets for Photodetectors, Acs Applied Nano Materials 4 (5) (2021) 5522–5530.
[48] D. Bahamon, M. Khalil, A. Belabbes, Y. Alwahedi, L.F. Vega, K. Polychronopoulou, A DFT study of the adsorption energy and electronic interactions of the SO2 molecule on a CoP hydrotreating catalyst, RSC Adv. 11 (5) (2021) 2947–2957.
[49] A. Zaman, R. Shahriar, S.M.T. Hossain, R. Akhond, H.T. Mumu, A. Sharif, A graphene-like BeS monolayer as a promising gas sensor material with strain and electric field induced tunable response: a first-principles study, RSC Adv. 13 (34) (2023) 23558–23569.
[50] C.X. Zhao, J.N. Liu, B.Q. Li, D. Ren, X. Chen, J. Yu, Q. Zhang, Multiscale Construction of Bifunctional Electrocatalysts for Long-Lifespan Rechargeable Zinc-Air Batteries, Adv. Funct. Mater. 30 (36) (2020) 9.
[51] M.A. Blanco, E. Francisco, V. Luaña, GIBBS: isothermal-isobaric thermodynamics of solids from energy curves using a quasi-harmonic Debye model, Comput. Phys. Commun. 158 (1) (2004) 57–72.
[52] A. Otero-de-la-Roza, V. Luaña, GIBBs2: A new version of the quasi-harmonic model code. I. Robust treatment of the static data, Comput. Phys. Commun. 182 (8) (2011) 1708–1720.
[53] S.R. Das, K. Wakabayashi, K. Tsukagoshi, S. Dutta, Ab-initio investigation of preferential triangular self-formation of oxide heterostructures of monolayer WSe2, Sci Rep 10 (1) (2020) 6.
[54] S.R. Das, K. Wakabayashi, M. Yamamoto, K. Tsukagoshi, S. Dutta, Layer-by-Layer Oxidation Induced Electronic Properties in Transition-Metal Dichalcogenides, J. Phys. Chem. C 122 (29) (2018) 17001–17007.
[55] H.B. Shu, M.L. Zhao, M.L. Sun, Theoretical Study of GaN/BP van der Waals Nanocomposites with Strain-Enhanced Electronic and Optical Properties for Optoelectronic Applications, Acs Applied Nano Materials 2 (10) (2019) 6482–6491.
[56] Y.Z. Wang, T. Liu, W.Z. Tian, Y. Zhang, P.Y. Shan, Y.J. Chen, W.H. Wei, H.K. Yuan, H. Cui, Mechanism for hydrogen evolution from water splitting based on a MoS2/WSe2 heterojunction photocatalyst: a first-principle study, RSC Adv. 10 (67) (2020) 41127–41136.
[57] S.K. Wang, H.Y. Tian, C.D. Ren, J. Yu, M.L. Sun, Electronic and optical properties of heterostructures based on transition metal dichalcogenides and graphene-like zinc oxide, Sci Rep 8 (2018).
[58] F.L. Ling, W. Kang, H.R. Jing, W. Zeng, Y.K. Chen, X.Q. Liu, Y.X. Zhang, L. Qi, L. Fang, M. Zhou, Enhancing hydrogen evolution on the basal plane of transition metal dichacolgenide van der Waals heterostructures. *npj Comput*, Mater. 5 (2019) 7.
[59] M.L. Sun, J.P. Chou, J. Yu, W.C. Tang, Effects of structural imperfection on the electronic properties of graphene/WSe2 heterostructures, Journal of Materials Chemistry C 5 (39) (2017) 10383–10390.
[60] S.K. Wang, C.D. Ren, H.Y. Tian, J. Yu, M.L. Sun, MoS2/ZnO van der Waals heterostructure as a high-efficiency water splitting photocatalyst: a first-principles study, Phys. Chem. Chem. Phys. 20 (19) (2018) 13394–13399.